

# PHASE-RESOLVED STUDIES OF THE HIGH-ENERGY GAMMA-RAY EMISSION FROM THE CRAB, GEMINGA, AND VELA PULSARS

J. M. FIERRO, P. F. MICHELSON, AND P. L. NOLAN

W. W. Hansen Experimental Physics Laboratory, Stanford University, Stanford, CA 94305-4085

AND

D. J. THOMPSON

NASA/Goddard Space Flight Center, Code 661, Greenbelt, MD 20771

Received 1997 February 20; accepted

## ABSTRACT

Using the first 3.5 years of observations from the Energetic Gamma Ray Telescope (EGRET) on board the *Compton Gamma Ray Observatory*, phase-resolved analyses are performed on the emission from the three brightest high-energy  $\gamma$ -ray pulsars: Crab, Geminga, and Vela. For each pulsar, it is found that there is detectable high-energy  $\gamma$ -ray emission above the galactic diffuse background throughout much of the pulsar rotation cycle. A hardness ratio is introduced to characterize the evolution of the spectral index as a function of pulsar phase. While the hardest emission from the Crab and Vela pulsars comes from the bridge region between the two  $\gamma$ -ray peaks, the hardest emission from Geminga corresponds to the second  $\gamma$ -ray peak. For all three pulsars, phase-resolved spectra of the pulse profile components reveal that although there is a large variation in the spectral index over the pulsar phase interval, the high-energy spectral turnover, if any, occurs at roughly the same energy in each component. The high-energy  $\gamma$ -ray emission from the Crab complex appears to include an unpulsed ultrasoft component of spectral index  $\sim -4.3$ , which dominates the total emission below 100 MeV. This component is consistent with the expected emission from the tail end of the Crab Nebula synchrotron emission.

*Subject headings:* gamma rays: observations — pulsars: individual (Crab, Geminga, Vela)

## 1. INTRODUCTION

High-energy  $\gamma$ -ray pulsars have proven to have complex, often extended, pulse profiles. By extracting only those photons that arrive during a specified phase interval, the emission characteristics of an individual pulse profile component can be determined, providing that there are sufficient photon statistics. Fortunately, the three brightest compact sources in the  $\gamma$ -ray sky are the high-energy  $\gamma$ -ray pulsars Crab (PSR B0531+21), Geminga (PSR J0633+1746), and Vela (PSR B0833–45). The spectral properties of the pulse profile components from these pulsars have been investigated previously using data from both *COS B* (Clear et al. 1987; Grenier, Hermesen, & Clear 1988) and EGRET (Nolan et al. 1993; Kanbach et al. 1994; Mayer-Hasselwander et al. 1994).

The earlier analyses for Crab and Vela compared the angular distribution of the data with the instrument point-spread distribution to define the source flux; no use was made of a detailed background model. Thus, the nonsource background level was not well determined. In the Geminga analysis by Mayer-Hasselwander et al. (1994), the nonsource background in the pulse profile was determined by spatial (cross-correlation) analysis of the counts in the off-pulse phase interval, simultaneously accounting for the model-predicted diffuse emission. In the present analysis, the increase in photon statistics available through the first 3.5 years of EGRET observations allows 20 phase intervals to be analyzed individually for all three pulsars by a spatial analysis procedure based on the maximum likelihood concept (Mattox et al. 1996), where the nonsource background has been accounted for on the basis of an improved model of the diffuse emission (Hunter et al. 1997). Some differences from earlier results may be caused by differences

in the analysis techniques. Within this analysis, each pulsar is analyzed by the same procedure, making the results directly comparable.

An improved knowledge of the emission characteristics as a function of pulsar rotation phase will lead to a better understanding of the emission processes and pulsar geometries responsible for modulated high-energy  $\gamma$ -rays. In particular, the phase-resolved behavior may be used to discriminate between the two most popular classes of models for pulsed high-energy  $\gamma$ -radiation: the polar cap models (see, e.g., Daugherty & Harding 1994, 1996; Sturmer, Dermer, & Michel 1995; Sturmer 1995), which propose that  $\gamma$ -rays result from energetic charged particles accelerated along the magnetic field lines just above the polar cap surfaces, and the outer gap models (see, e.g., Cheng et al. 1986a, 1986b; Romani & Yadigaroglu 1995; Yadigaroglu & Romani 1995), in which it is postulated that  $\gamma$ -rays are produced by charged particles accelerated in vacuum gaps formed in the outer regions of the pulsar magnetosphere. Polar cap  $\gamma$ -radiation should be narrowly beamed in the same direction as the radio emission, with a possible high-energy cutoff in the photon spectrum due to attenuation by the strong magnetic field near the polar cap surface. The outer gap  $\gamma$ -ray beam is expected to be broad and complex, consisting of emission generated along the last closed field lines.

This paper examines the phase-resolved emission characteristics of the three brightest high-energy  $\gamma$ -ray pulsars: Crab, Vela, and Geminga. A limited phase-resolved analysis of the high-energy  $\gamma$ -ray emission from PSR B1706–44 is presented by Thompson et al. (1996). The remaining two pulsars detected by EGRET, PSR B1055–52 and PSR B1951+32, do not yet have sufficient photon counting sta-

tistics to perform a meaningful phase-resolved study of their emission (Fierro 1995).

## 2. OBSERVATIONS

EGRET is sensitive to  $\gamma$ -rays in the energy range from  $\sim 30$  MeV to  $\sim 30$  GeV. The EGRET instrument and its calibration have been described extensively in Hughes et al. (1980), Kanbach et al. (1988, 1989), Nolan et al. (1992), and Thompson et al. (1993). EGRET records each  $\gamma$ -ray as an electron-positron pair production event. This event is processed automatically to determine the optimal estimate of arrival direction and energy of the photon (Bertsch et al. 1989). The arrival time of each photon is recorded in Universal Coordinated Time (UTC) with an absolute timing accuracy of better than  $100 \mu\text{s}$ . Because of the very low flux level of high-energy  $\gamma$ -rays, observing periods typically last about two weeks.

This paper considers the combined observations made during the first three cycles of the *Compton Gamma-Ray Observatory* mission, which lasted from 1991 April to 1994 October. As shown by Ramanamurthy et al. (1995b), Mayer-Hasselwander et al. (1994), and McLaughlin et al. (1996), these pulsars show no evidence of strong variability. The present data include the results of the in-flight calibration analysis of EGRET (Esposito et al. 1998). This analysis added a small energy-dependent correction after the data set used by Ramanamurthy et al. (1995b) was complete.

The photon arrival times were transformed to solar system barycentric time,  $T$ , and the corresponding rotational phases,  $\phi$ , for each pulsar were determined by taking the

fractional part of the Taylor expansion,

$$\phi(T) = \phi(T_0) + f_0(T - T_0) + \frac{1}{2}f_1(T - T_0)^2 + \frac{1}{6}f_2(T - T_0)^3, \quad (1)$$

where  $f_0$ ,  $f_1$ , and  $f_2$  are the pulsar spin frequency and first two time derivatives measured at the reference epoch  $T_0$ . The ephemerides used for the temporal analysis of the Crab, Geminga, and Vela pulsars are listed in Tables 1, 2, and 3, respectively. The epoch is given in units of Modified Julian Days (MJD = JD - 2400000.5). The Crab and Vela timing solutions are made available via the regularly updated Princeton Pulsar Timing Database and its associated corrections for dispersion measure drifts (Arzoumanian et al. 1992). The value of  $\Delta T_\oplus$  listed in the last column of Tables 1 and 3 is the amount of time after  $0^{\text{h}}$  UTC on the epoch day that a main radio pulse would arrive at the center of the Earth if there were no dispersion delays. This quantity is used to determine  $\phi(T_0)$  in equation (1). Since Geminga is not a radio pulsar, its timing solution is derived using a “ $Z_n^2$  timing method” based on the first 4 years of EGRET observations (Mattox 1994; J. R. Mattox 1995, private communication). The frequency second derivative,  $f_2$ , of Geminga is too small to be measured and is set equal to zero.

## 3. PHASE-RESOLVED SPATIAL ANALYSIS

Analysis of  $\gamma$ -ray point sources in the EGRET data set is typically performed using a maximum likelihood technique (Mattox et al. 1996), in which a  $\gamma$ -ray excess above the predicted background emission is required to be spatially distributed as the instrument point-spread function before

TABLE 1  
RADIO TIMING PARAMETERS OF THE CRAB PULSAR

Valid Dates	$T_0$ (MJD)	$f_0$ ( $\text{s}^{-1}$ )	$f_1$ ( $10^{-10} \text{ s}^{-2}$ )	$f_2$ ( $10^{-20} \text{ s}^{-3}$ )	$\Delta T_\oplus$ (ms)
1991 Mar 16–Jun 5 .....	48,371	29.9492515379593	−3.77657	0.818	8.3
1991 May 30–Aug 25 .....	48,449	29.9467067038240	−3.77575	1.06	23.8
1992 Jun 28–Oct 18 .....	48,857	29.9334039601096	−3.77156	1.16	1.5
1992 Dec 27–1993 Apr 11 .....	49,035	29.9276050289288	−3.76972	1.05	25.8
1993 Apr 6–Jul 5 .....	49,128	29.9245763662884	−3.76877	1.01	15.5
1993 Nov 5–1994 Jan 27 .....	49,337	29.9177729429376	−3.76650	1.32	23.0
1993 Dec 19–1994 Feb 28 .....	49,375	29.9165363960966	−3.76612	0.921	4.9
1994 Jun 23–Nov 15 .....	49,598	29.9092823758179	−3.76380	1.30	26.3

TABLE 2  
TIMING PARAMETERS FOR THE GEMINGA PULSAR

Valid Dates	$T_0$ (MJD)	$f_0$ ( $\text{s}^{-1}$ )	$f_1$ ( $\text{s}^{-2}$ )	$f_2$ ( $\text{s}^{-3}$ )
1989 Jul 8–1996 Apr 24 .....	48,750	4.2176690940300	$-1.95206 \times 10^{-13}$	$< 6 \times 10^{-24}$

TABLE 3  
RADIO TIMING PARAMETERS OF THE VELA PULSAR

Valid Dates	$T_0$ (MJD)	$f_0$ ( $\text{s}^{-1}$ )	$f_1$ ( $10^{-11} \text{ s}^{-2}$ )	$f_2$ ( $10^{-21} \text{ s}^{-3}$ )	$\Delta T_\oplus$ (ms)
1991 Feb 1–May 22 .....	48,343	11.1988875613749	−1.55793	1.18	66.2
1991 Aug 12–Sep 29 .....	48,504	11.1987003711301	−1.56791	4.17	22.3
1991 Oct 21–1992 Jan 16 .....	48,593	11.1985799537572	−1.56584	2.25	93.3
1993 Apr 1–Aug 8 .....	49,142	11.1978384490139	−1.56166	0.876	84.3
1993 Jul 1–Aug 27 .....	49,197	11.1977642483505	−1.56105	3.88	63.5
1993 Sep 16–Nov 20 .....	49,278	11.1976550192558	−1.56063	1.08	84.8
1994 Aug 28–Sep 23 .....	49,605	11.1972260134043	−1.56636	0.626	69.7

being considered as point-source emission. In the EGRET energy range, the  $\gamma$ -ray background is assumed to consist of an isotropic, extragalactic component and Galactic diffuse emission due primarily to cosmic-ray particles interacting with matter and fields in the Galaxy (Bertsch et al. 1993; Hunter et al. 1997). Although the background model does not provide an adequate global fit to the all-sky data, it is an acceptable representation of the sky brightness in limited regions if the strengths of the galactic and extragalactic components are treated as adjustable parameters.

The Crab, Vela, and Geminga pulsars have sufficient  $\gamma$ -ray counting statistics that it is possible to restrict the spatial analysis to photons arriving during a specific phase interval, which allows the absolute emission levels to be determined across the pulse profile.

The likelihood analysis is subject to small systematic uncertainties (Mattox et al. 1996), including inaccuracies in the assumed diffuse model, assumptions made about other sources in the field of view, and limitations of the EGRET calibration data. Thompson et al. (1995), for example, recommend a 10% systematic uncertainty be associated with any absolute number, and McLaughlin et al. (1996) find that a 6% systematic uncertainty is sufficient to justify the assumption that the pulsars are not varying. For comparisons between different phases of a given pulsar, these systematic uncertainties can be neglected because all phases are analyzed under the same conditions.

For each of the three bright  $\gamma$ -ray pulsars, the pulse profile is divided into 20 phase bins of equal width ( $\Delta\phi = 0.05$ ), and likelihood analysis is performed on the 20 resulting spatial photon counts maps. There are not enough counts to perform a full spectral analysis for each of the 20 phase bins. Instead, a *hardness ratio*,  $R$ , is defined as

$$R \equiv \frac{F(> 300 \text{ MeV})}{F(100\text{--}300 \text{ MeV})}, \quad (2)$$

where  $F(100\text{--}300 \text{ MeV})$  is the likelihood flux measured between 100 and 300 MeV, and  $F(> 300 \text{ MeV})$  is the likelihood flux measured above 300 MeV, both in units of photons per square centimeter per second. A source with a differential flux behaving as a perfect power law above 100 MeV with a spectral index of  $-2.0$  will have a hardness ratio of  $R \simeq 0.5$ .

### 3.1. The Crab Pulsar

Analysis of the Crab region is complicated by the fact that a solar flare bright enough to be detected by EGRET as a strong source occurred on 1991 June 11 (Kanbach et al. 1993), when the Sun was in a direction only  $\sim 4.4^\circ$  from that of the Crab pulsar. Rather than introduce possible errors by trying to account for the solar flare emission, all photons arriving during the  $\sim 8.5$  hr flare period are excluded from the Crab pulsar analysis.

The results of the phase-resolved spatial likelihood analysis of the Crab pulse profile are shown graphically in Figure 1. The top panel shows the traditional phase histogram above 100 MeV formed by epoch-folding all events from the first three cycles of EGRET observations arriving within an energy-dependent cone of half-angle  $\theta_{67} = 5.85^\circ \times (E_\gamma/100 \text{ MeV})^{-0.534}$  about the pulsar position, where  $E_\gamma$  is the measured photon energy. This cone accepts  $\sim 67\%$  of the photons that EGRET detects from a point source (Thompson et al. 1993). The phase interval has been divided

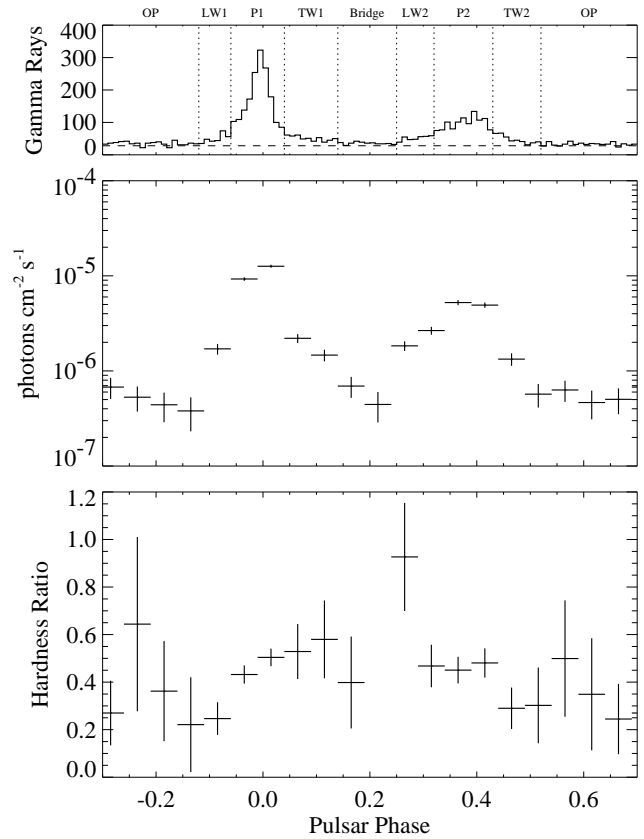


FIG. 1.—Phase-resolved likelihood analysis of the Crab pulse profile. *Top*: The  $\gamma$ -ray phase histogram above 100 MeV formed from the data accumulated during the first three cycles of EGRET observations. The vertical dashed lines indicate the definitions of the pulse profile components listed in Table 4. The histogram consists of 100 phase bins. The pulsar phase is defined so that the main radio peak occurs at zero. The horizontal dashed line shows the level of nonsource gamma radiation expected, based on spatial analysis of the off-pulse region. *Middle*: Instantaneous photon flux above the diffuse background level as derived from the spatial likelihood analysis of each phase bin for energies greater than 100 MeV. *Bottom*: Hardness ratios as defined by eq. (2).

into the eight components defined in Table 4, indicated by vertical dashed lines in the top panel of Figure 1. These boundary intervals differ from those of Clear et al. (1987) and Nolan et al. (1993) because the increase in data has allowed features to be resolved on a finer scale. The horizontal, dashed line represents the nonsource background gamma radiation within this cone, determined as follows: The off-pulse phase region was analyzed using the maximum likelihood method to calculate the number of photons associated with the Crab. Of these, 67% should be in the light curve. The nonsource background is then the difference between the total number of photons and the

TABLE 4

CRAB PULSAR PHASE INTERVAL DEFINITIONS

Component	Phase Interval
Leading wing 1 (LW1).....	0.88–0.94
Peak 1 (P1) .....	0.94–0.04
Trailing wing 1 (TW1).....	0.04–0.14
Bridge .....	0.14–0.25
Leading wing 2 (LW2).....	0.25–0.32
Peak 2 (P2) .....	0.32–0.43
Trailing wing 2 (TW2).....	0.43–0.52
Off-pulse (OP).....	0.52–0.88

number of source photons expected in this part of the light curve. This method is similar to the one used by Mayer-Hasselwander et al. (1994) for Geminga.

The center panel of Figure 1 shows the instantaneous photon flux above 100 MeV measured for each of the 20 phase bins. The total level of emission from the Crab pulsar is the average of the plotted values. The error bars represent the  $1\sigma$  statistical uncertainty levels. The values are plotted on a logarithmic scale because the photon flux varies by almost 2 orders of magnitude across the pulse profile, with the single bin centered about the first peak accounting for  $\sim 35\%$  of the total Crab emission. Unlike the phase histogram shown in the top panel, the center plot shows only the emission above the predicted  $\gamma$ -ray background level. Significant point-source emission is detected from the Crab region over almost the entire pulse profile. The low bin, centered on phase  $-0.15$ , has statistical significance of only  $2.5\sigma$ , an excess of 27 photons on the expected nonsource emission of 140. All the other bins have significance greater than  $3.5\sigma$ .

Previous studies of the high-energy  $\gamma$ -ray emission from the Crab complex (Clear et al. 1987; Nolan et al. 1993; Ramanamurthy et al. 1995b; de Jager et al. 1996) have treated the emission in the off-pulse (OP) region of the pulse profile as an unpulsed component due entirely to the Crab Nebula. This is in analogy with observational results at lower energies, where the total Crab luminosity is dominated by the nebular contribution. Unlike detectors at lower energies, however, current  $\gamma$ -ray telescopes do not have sufficient angular resolution to separate the pulsar radiation from any possible nebular emission. As will be shown in the following sections, it is very likely that much of the emission in the off-pulse phase interval comes from the pulsar itself. It is noteworthy that the photon flux level measured for the phase bin at  $\phi \approx 0.2$  is comparable to the flux level measured over the off-pulse phase interval. It had been assumed that the emission throughout the bridge region was well above the off-pulse emission level. An unpulsed component present in the Crab pulse profile can be no greater than flux measured in the weakest phase bin. Thus, an unpulsed component has a maximum flux of  $(3.8 \pm 1.5) \times 10^{-7}$  photons  $\text{cm}^{-2} \text{s}^{-1}$  or  $16\% \pm 8\%$  of the total Crab emission above 100 MeV.

The lower panel of Figure 1 plots the hardness ratios calculated for the same set of phase bins. There is no data point plotted for the bin centered at phase  $\phi \approx -0.15$  because the paucity of counts in that bin prevented a detection in the 100–300 MeV energy range. The most striking aspect of this plot is the absence of a strong correlation to the features in the pulse profile. The hardness ratio increases smoothly as the pulsar phase moves across the first pulse, leveling out in the bridge region before reaching its maximum value in the leading wing of the second peak ( $\phi \approx 0.25$ ). A weak detection of this bin in the 100–300 MeV energy range leads to the relatively large error bar. As the phase increases through the second peak, the hardness ratio decreases back to the soft level of the off-pulse emission. It is interesting that the extreme hardness ratios are in the bridge and off-pulse phase intervals, not near the two peaks that dominate the pulsar light curve.

### 3.2. The Geminga Pulsar

The phase histogram, phase-resolved instantaneous flux, and hardness ratio distribution of the Geminga pulsar are

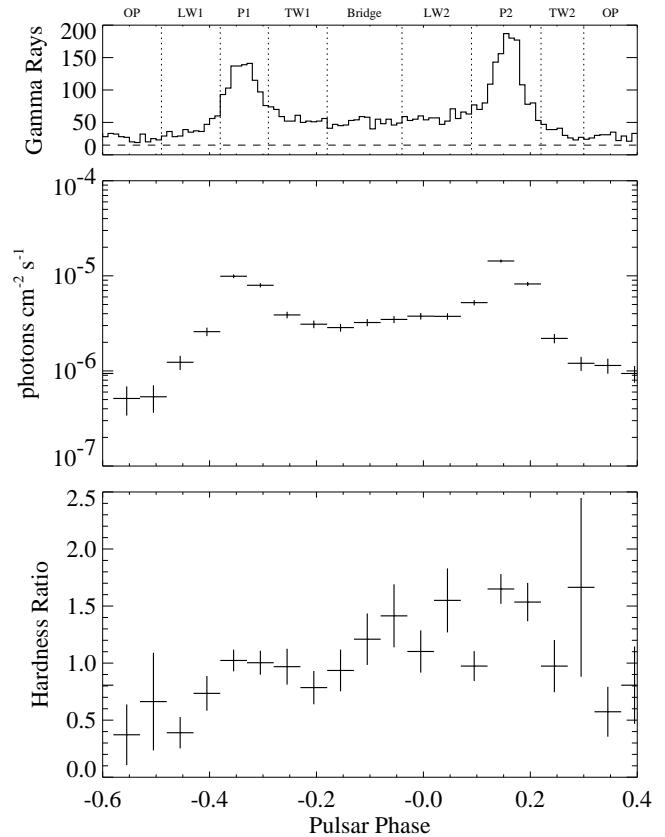


FIG. 2.—Phase-resolved likelihood analysis of the Geminga pulse profile. *Top*: The  $\gamma$ -ray phase histogram above 100 MeV, with the vertical dashed lines indicating the definitions of the pulse profile components listed in Table 5. The histogram consists of 100 phase bins. The pulsar phase is relative to the timing epoch. The horizontal dashed line shows the level of nonsource gamma radiation expected, based on spatial analysis of the off-pulse region. *Middle*: instantaneous photon flux above the diffuse background level for energies greater than 100 MeV. *Bottom*: hardness ratios.

shown in Figure 2. The vertical, dashed lines in the top panel indicate the definitions of the pulse profile components listed in Table 5, and the horizontal dashed line shows the nonsource background emission, calculated in the same way as for the Crab. Note that the dashed line is close to the observed points in the phase region leading the first pulse (see also Fig. 2 of Mayer-Hasselwander et al. 1994). The plot of the instantaneous flux level above 100 MeV shows that Geminga has an even higher average level

TABLE 5

GEMINGA PULSAR PHASE INTERVAL DEFINITIONS

Component	Phase Interval
Leading wing 1 (LW1).....	0.51–0.62
Peak 1 (P1) .....	0.62–0.71
Trailing wing 1 (TW1).....	0.71–0.82
Bridge .....	0.82–0.96
Leading wing 2 (LW2).....	0.96–0.09
Peak 2 (P2) .....	0.09–0.22
Trailing wing 2 (TW2).....	0.22–0.30
Off-pulse (OP) .....	0.30–0.51

of off-pulse emission than does the Crab. However, unlike the Crab pulsar, Geminga has no known nebular association, and it must be assumed that the high level of emission seen throughout most of the pulse profile is coming directly from the pulsar, as noted previously by Mayer-Hasselwander et al. (1994). The flux at phase  $\phi \approx -0.55$  is about one-third the emission measured from either of the adjacent phase bins, and, even considering the large uncertainties, represents a significant drop in intensity. This statistical significance of this bin is less than  $2.5 \sigma$ , so this point should conservatively be treated as an upper limit. Any unpulsed component to the total Geminga emission cannot be stronger than the flux level of  $(5.1 \pm 1.7) \times 10^{-7}$  photons  $\text{cm}^{-2} \text{s}^{-1}$  measured in this bin. This corresponds to  $14\% \pm 7\%$  of the total Geminga emission. As opposed to the Crab pulsar, the emission level over the entire bridge region of the Geminga pulse profile is much higher than the off-pulse emission level. Except for the one low bin, all of the phase regions show excesses at a statistical significance greater than  $5 \sigma$ .

The distribution of the Geminga hardness ratios, plotted in the lower panel of Figure 2, appears to be correlated to the basic features of the  $\gamma$ -ray pulse profile. There is perhaps a local maximum in the hardness ratio at the location of the first peak, with even harder emission in the latter part of the bridge region and the second peak. In general, the Geminga hardness ratios are much higher than those measured for the Crab pulsar.

### 3.3. The Vela Pulsar

Figure 3 shows the phase histogram, phase-resolved flux, and hardness ratios for the Vela pulsar, with the pulse profile components defined in Table 6 indicated by vertical, dashed lines in the top panel. The horizontal dashed line shows the nonsource background emission, calculated in the same way as for the Crab. The increased statistics and complicated morphology of the Vela pulse profile allows for the introduction of two additional components not defined by Kanbach et al. (1994). For lack of better names, these have been denoted as “interpulse 1” (IP1) and “interpulse 2” (IP2), and they correspond to the slight plateau after the first peak and its trailing edge, respectively. These are not to be confused with radio pulsar astronomers’ use of the term “interpulse” to denote the weaker pulse in a two-pulse profile.

The instantaneous flux of Vela shown in the center panel of Figure 3 exhibits a greater variation as a function of pulsar phase than either the Crab or Geminga pulsars. The measured instantaneous flux above 100 MeV exceeds

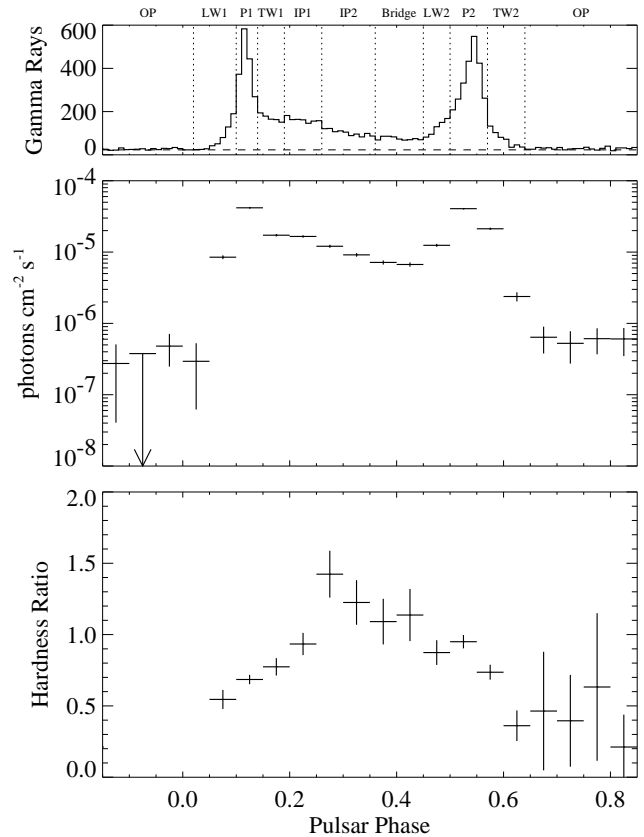


FIG. 3.—Phase-resolved likelihood analysis of the Vela pulse profile. *Top*: The  $\gamma$ -ray phase histogram above 100 MeV, with the vertical dashed lines indicating the definitions of the pulse profile components listed in Table 6. The histogram consists of 100 phase bins. The pulsar phase is defined so that the main radio peak occurs at zero. The horizontal dashed line shows the level of nonsource gamma radiation expected, based on spatial analysis of the off-pulse region. *Middle*: instantaneous photon flux above the diffuse background level for energies greater than 100 MeV. *Bottom*: the hardness ratios.

$4 \times 10^{-5}$  photons  $\text{cm}^{-2} \text{s}^{-1}$  for both peaks, almost 20 times the average intensity from Crab, which reflects the fact that Vela is the brightest compact object in the  $\gamma$ -ray sky. Although seven of the eight phase bins in the off-pulse region have a measured flux above the diffuse background, none of the individual bins in the off-pulse region measure strong detections, and one of the bins has only an upper limit. This contrasts strongly with the Crab and Geminga pulsars, which show significant emission over most of the pulsar phase. A likelihood analysis of the entire off-pulse phase region,  $0.64\text{--}0.02$ , finds a point-source signal at a  $5.6 \sigma$  confidence level and an instantaneous flux of  $(4.4 \pm 0.9) \times 10^{-7}$  photons  $\text{cm}^{-2} \text{s}^{-1}$ . Thus, there is evidence that Vela has emission beyond the phase region traditionally associated with the pulsar, even though the data do not justify the claim that the emission extends throughout the full rotation. If this level of emission is assumed to be present throughout the pulse profile, it represents only  $4.4\% \pm 0.9\%$  of the total emission, which does not conflict with the upper limits to unpulsed emission established by Grenier et al. (1988) or Kanbach et al. (1994). Even though the flux levels measured in the off-pulse regions of the Crab and Vela pulsars are comparable, the Vela flux values have larger uncertainties because the EGRET exposure to Vela

TABLE 6

VELA PULSAR PHASE INTERVAL DEFINITIONS	
Component	Phase Interval
Leading wing 1 (LW1).....	0.02–0.10
Peak 1 (P1) .....	0.10–0.14
Trailing wing 1 (TW1).....	0.14–0.19
Interpulse 1 (IP1) .....	0.19–0.26
Interpulse 2 (IP2) .....	0.26–0.36
Bridge .....	0.36–0.45
Leading wing 2 (LW2).....	0.45–0.50
Peak 2 (P2) .....	0.50–0.57
Trailing wing 2 (TW2).....	0.57–0.64
Off-pulse (OP) .....	0.64–0.02

was  $\sim 2/3$  that of the Crab over the first three cycles of instrument operation.

The lower panel of Figure 3 shows the distribution of hardness ratios across the Vela pulse profile. The weak level of off-pulse emission combined with the limited EGRET exposure to Vela prevented a useful determination of hardness ratios over the phase range 0.85–0.05. The phase evolution of the Vela hardness ratio is reminiscent of the behavior of the Crab hardness ratio (Fig. 1). As with the Crab pulsar, the Vela emission becomes harder as the phase moves through the first peak and softer as the phase increases past the second peak into the off-pulse component.

#### 4. PHASE-RESOLVED SPECTRA

To further investigate the implied spectral variation as a function of rotation phase implied by the hardness ratio distributions of the three bright  $\gamma$ -ray pulsars, differential photon spectra over the EGRET energy range are derived for the various pulsar components defined in Tables 4, 5, and 6. Each component spectrum is derived by performing standard likelihood spatial analysis (Mattox et al. 1996) in 10 independent energy intervals using only those photons within the corresponding phase range. As noted by Esposito et al. (1998), the EGRET in-flight calibration checks showed that the original calibration below 70 MeV was in error. The corrections necessarily introduce larger uncertainties in the 30–50 MeV and 50–70 MeV data points than found in the other energy bins.

##### 4.1. The Crab Pulsar

The photon spectrum derived from likelihood spatial analysis of the total Crab emission is shown in Figure 4 for the energy range 30 MeV–10 GeV. Likelihood analysis is not performed above 10 GeV because the low photon statistics make it difficult to perform effective maximum likelihood parameter estimation (see Mattox et al. 1996). As indicated by the solid line in Figure 4, the Crab differential photon spectrum,  $dN/dE$ , is consistent with a power law of index  $\alpha = -2.12 \pm 0.03$  over the energy range 100 MeV–10 GeV, similar to the results of Nolan et al. (1993) and

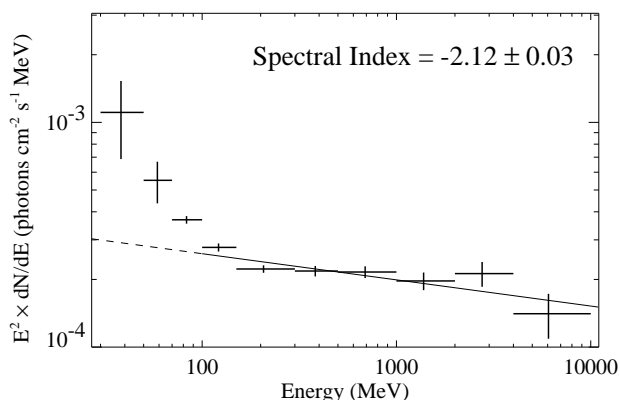


FIG. 4.—Photon spectrum of the total emission from Crab derived using spatial analysis. The power-law fit is to the data points between 100 MeV and 10 GeV, with the dashed line indicating the extrapolated power law down to 30 MeV. The spectral index refers to the differential photon spectrum,  $dN/dE$ .

Ramanamurthy et al. (1995b). However, the first three energy bins from 30–100 MeV deviate significantly from the trend established by the higher energy bins. A spectral power-law fit including all 10 energy bins results in a  $\chi^2$  value of 47.5 with 8 degrees of freedom (dof), which implies that the probability that the 10 measured values are drawn from a photon spectrum behaving as a simple power law over the entire EGRET energy range is  $1.2 \times 10^{-7}$ . Even the restricted fit above 100 MeV measures a  $\chi^2$  of 10.7 for 5 dof, which corresponds to a probability of 5.9%.

Figure 5 shows the instantaneous photon spectra derived from likelihood analysis of the phase intervals defined in Table 4. The time-averaged spectra are obtained by multiplying the flux values by the phase width of each component. For each component, a spectral fit is performed only over the energy interval for which the data points were reasonably consistent with a power-law distribution. Not surprisingly, component spectra reflect many of the features suggested by the hardness plot of Figure 1. The softest components in the Crab light curve are the second pulse trailing wing (TW2), off-pulse (OP), and first pulse leading wing (LW1) components. The pulsar emission is hardest in the bridge and leading wing of the second pulse (LW2). The only component that shows some evidence of a high-energy turnover is the first peak (P1). Nevertheless, the absence of pulsed emission at teravolt energies (see, e.g., Vacanti et al. 1991) indicates that the pulsed emission must have a cutoff between the EGRET and teravolt energy ranges. Although based on more extensive data, the principal characteristics of the phase-resolved spectral components are similar to those found by Nolan et al. (1993) for the pulsed emission alone.

Much like the total spectrum of Figure 4, the first pulse trailing wing (TW1), bridge, LW2, and OP components all appear to have a softer spectrum at energies less than 100 MeV, which deviates from the power law established above 100 MeV. This implied spectral break is especially apparent for the bridge and off-pulse regions, the two weakest components of the Crab pulse profile. To investigate this behavior, the spectra are fit with a double power law of the form

$$\frac{dN}{dE} = I_1 E^{\alpha_1} + I_2 E^{\alpha_2} \text{ photons cm}^{-2} \text{ s}^{-1} \text{ MeV}^{-1}. \quad (3)$$

Figure 6 shows the double power-law fit to the total Crab emission, and Figure 7 shows similar fits to spectra of the TW1, bridge, LW2, and OP components. The various parameters of the double power-law fits are listed in Table 7. The  $\chi^2$  values listed in the sixth column indicate that the measured photon spectrum for each component in Table 7 is well modeled by emission from two independent power laws over the energy range, 30 MeV–10 GeV. The second and third columns of Table 7 show that the soft component is consistently fit with a spectral index of  $\alpha_1 \lesssim -4$  and a flux at 100 MeV of  $F_1(100 \text{ MeV}) \sim 10^{-8} \text{ photons cm}^{-2} \text{ s}^{-1}$ , while the fourth and fifth columns show that the harder high-energy emission varies for each component. This strongly suggests the presence of an unpulsed ultrasoft component to the Crab total emission that dominates the pulsar radiation from the weaker pulse profile components at energies less than  $\sim 100$  MeV.

##### 4.2. The Geminga Pulsar

The total Geminga spectrum plotted in Figure 8 is consistent with a power law from 30 MeV to 2 GeV of spectral

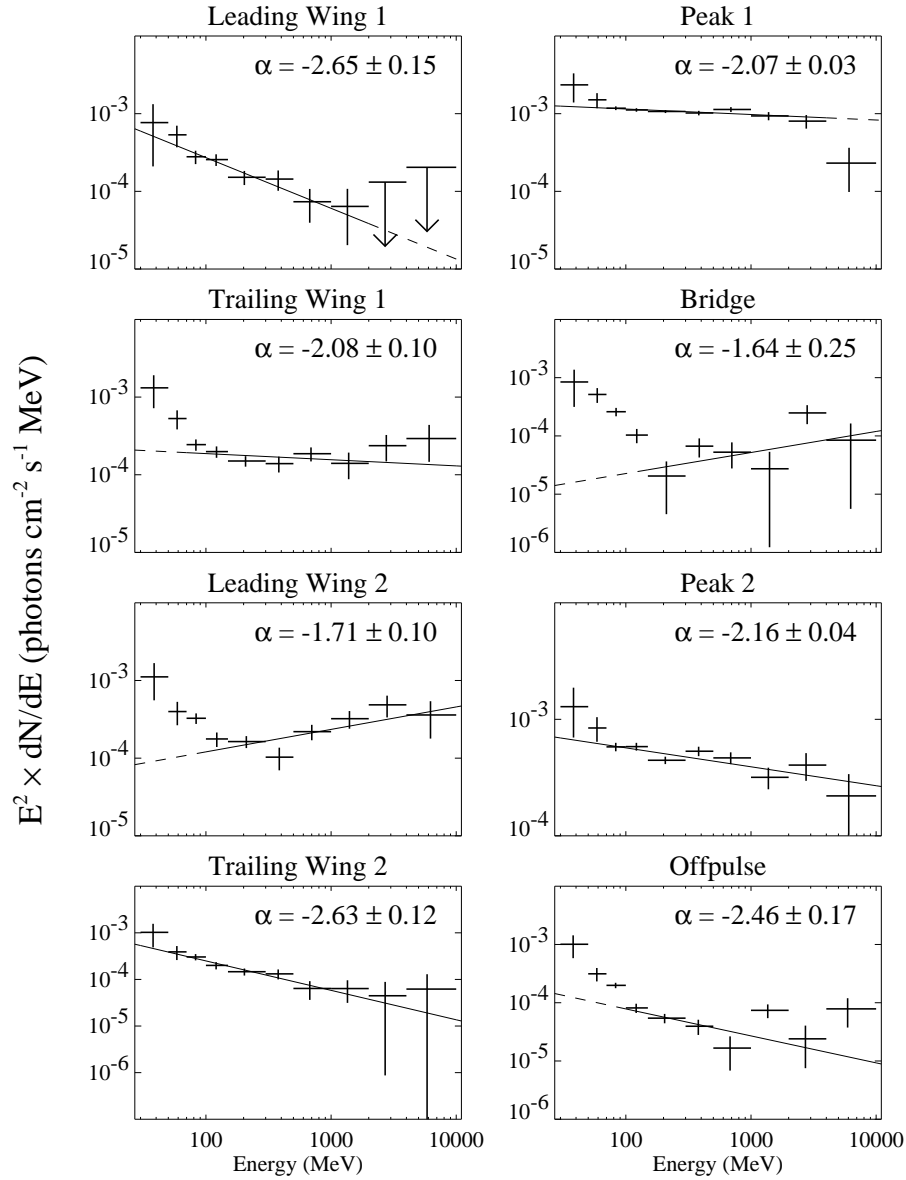


FIG. 5.—Instantaneous photon spectra derived from likelihood spatial analysis of the Crab pulse profile components defined in Table 4. The power-law fit is indicated by a solid line, with the differential spectral index  $\alpha$  listed for each component. The upper limits are  $2\sigma$ .

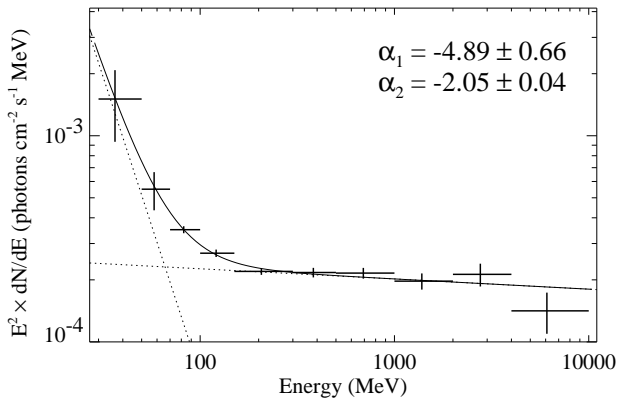


FIG. 6.—Double power-law fit to the total Crab emission photon spectrum. The fit has a form given by eq. (3). Dotted lines indicate the two independent power laws.

index  $-1.42 \pm 0.02$ . Besides being significantly harder and having no ultrasoft low-energy component, the Geminga total spectrum is much different than the Crab total spectrum in that it shows a sharp spectral turnover at high energies. The spectral result appears consistent with that of Mayer-Hasselwander et al. (1994), which indicates that the differences in analysis technique have no strong influence on the results.

The individual component spectra of Geminga are shown in Figure 9. With the exception of perhaps the TW2 and off-pulse phase intervals, all of the components show some indication of a turnover at high energies, typically around a few giga-electron volts. As is suggested by the distribution of hardness ratios, the P2 component has a significantly flatter spectrum than any of the other phase intervals. Indeed, it is the hardest spectrum yet measured by EGRET.

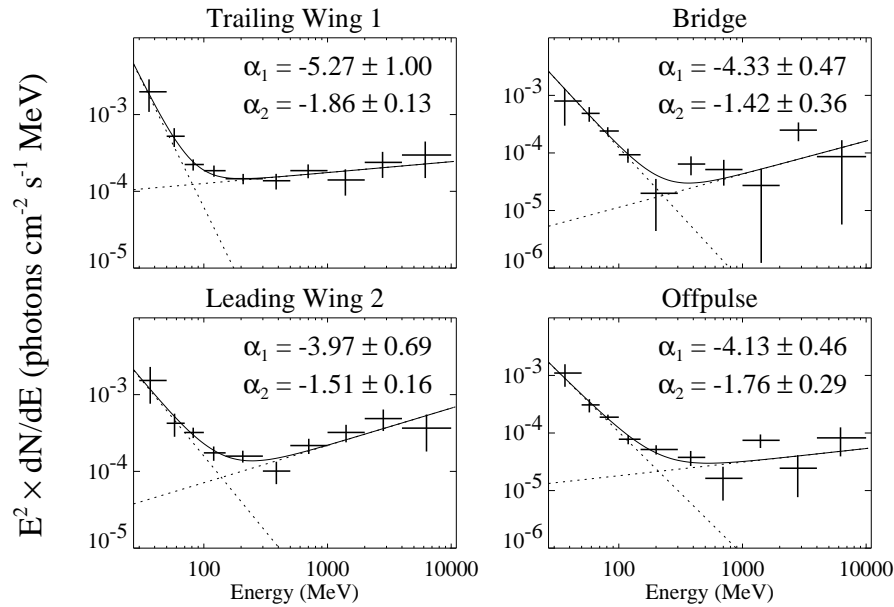


FIG. 7.—Double power-law fits to the likelihood-derived photon spectra of the TW1, bridge, LW2, and OP components of the Crab pulse profile

The softest components are the OP and LW1 phase intervals, which are also the only two components that are not detected at the highest energies. The LW1 and P1 components appear to exhibit the earliest and strongest spectral

turnovers. Again, these results are completely compatible with those of Mayer-Hasselwander et al. (1994), although the definitions of phase intervals are somewhat different.

#### 4.3. The Vela Pulsar

The Vela total photon spectrum is presented in Figure 10. Over the energy range 30–2000 MeV, the spectrum is consistent with a power law of index  $-1.62 \pm 0.01$ . Like Geminga, Vela exhibits a spectral turnover above  $\sim 1$  GeV. The shape of the spectrum is similar to that found by Kanbach et al. (1994), although the formal errors on the spectral index do not overlap. Some of this may be attributable to time-dependent corrections applied to the long-term EGRET database (Esposito et al. 1998) after the work of Kanbach et al. (1994). It may also reflect the fact that systematic uncertainties become important for a bright source like Vela, and such systematics are not shown in the statistical error bars. Although it may appear that the Vela spectrum is inconsistent with the fitted power law at energies below 70 MeV, the uncertainties associated with the flux values measured for the lowest two energy bins are large, and the deviations are not statistically significant. Nevertheless, the OSSE detection of unpulsed emission from the Vela synchrotron nebula in the 0.061 to  $\sim 4$  MeV

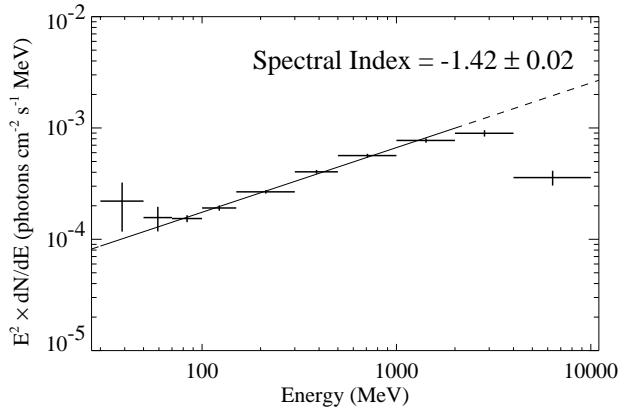


FIG. 8.—Photon spectrum of the total emission from Geminga derived using spatial analysis. The power-law fit is to the data points between 30 MeV and 2 GeV, with the dashed line indicating the extrapolated power law out to 10 GeV.

TABLE 7  
CRAB DOUBLE POWER-LAW SPECTRAL FITS

COMPONENT	POWER LAW 1		POWER LAW 2		$\chi^2(6 \text{ DOF})$
	$F_1(100 \text{ MeV})^a$	$\alpha_1$	$F_2(100 \text{ MeV})^a$	$\alpha_2$	
Total .....	$0.7 \pm 0.2$	$-4.89 \pm 0.66$	$2.3 \pm 0.3$	$-2.05 \pm 0.04$	11.04
TW1 .....	$0.6 \pm 0.4$	$-5.27 \pm 1.00$	$1.3 \pm 0.4$	$-1.86 \pm 0.13$	6.06
Bridge .....	$1.2 \pm 0.3$	$-4.33 \pm 0.47$	$0.1 \pm 0.1$	$-1.42 \pm 0.36$	10.26
LW2 .....	$1.6 \pm 0.4$	$-3.97 \pm 0.69$	$0.7 \pm 0.4$	$-1.51 \pm 0.16$	4.02
OP .....	$1.0 \pm 0.2$	$-4.13 \pm 0.46$	$0.2 \pm 0.2$	$-1.76 \pm 0.29$	2.40

<sup>a</sup> Modeled instantaneous differential flux at 100 MeV in units of  $10^{-8} \text{ photons cm}^{-2} \text{ s}^{-1} \text{ MeV}^{-1}$ .



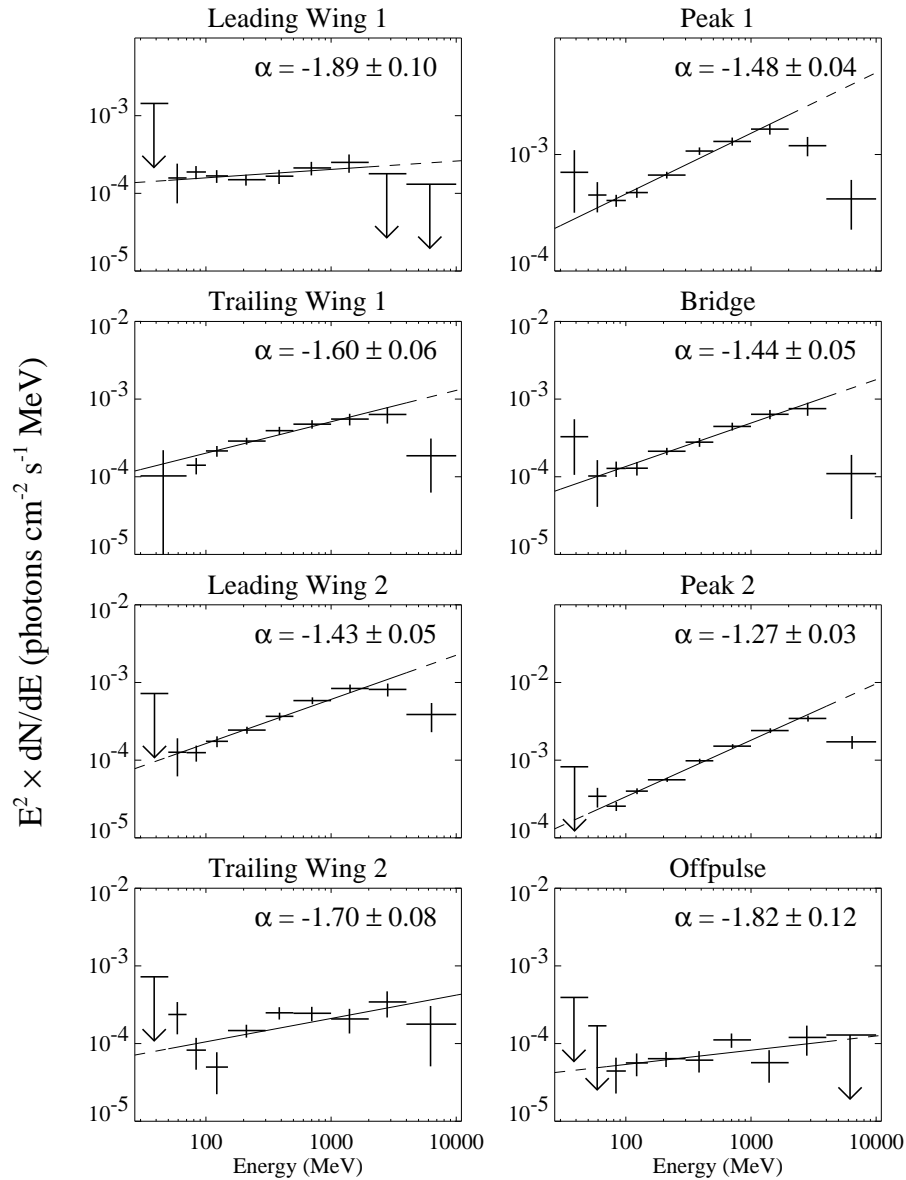


FIG. 9.—Instantaneous photon spectra derived from likelihood spatial analysis of the Geminga pulse profile components defined in Table 5

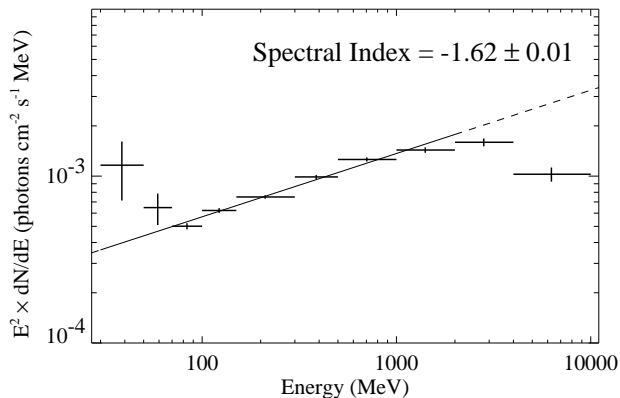


FIG. 10.—Photon spectrum of the total emission from Vela derived using spatial analysis. The power-law fit is to the data points between 30 MeV and 2 GeV, with the dashed line indicating the extrapolated power law out to 10 GeV.

range (de Jager, Harding, & Strickman 1996) indicates that there must be a turn up of the total Vela spectrum near or below the EGRET energy range. The low-energy EGRET points are consistent with the cutoff of the synchrotron spectrum near 40 MeV predicted by de Jager et al. (1996).

The instantaneous differential photon spectra of the components defined in Table 6 are presented in Figure 11. For the OP component, some energy bins had to be combined so that likelihood analysis could produce a reasonable flux estimate. Except for the OP interval, all of the Vela pulsar components show a turnover at energies on the order of a few giga-electron volts, with the LW1 and P1 spectra exhibiting the earliest deviations from power-law behavior. Only the TW2 component fails to produce a signal at the highest energies. The IP2 phase interval is the hardest component, as was suggested by the hardness ratio distribution of Figure 3. Although the phase bins do not match those of

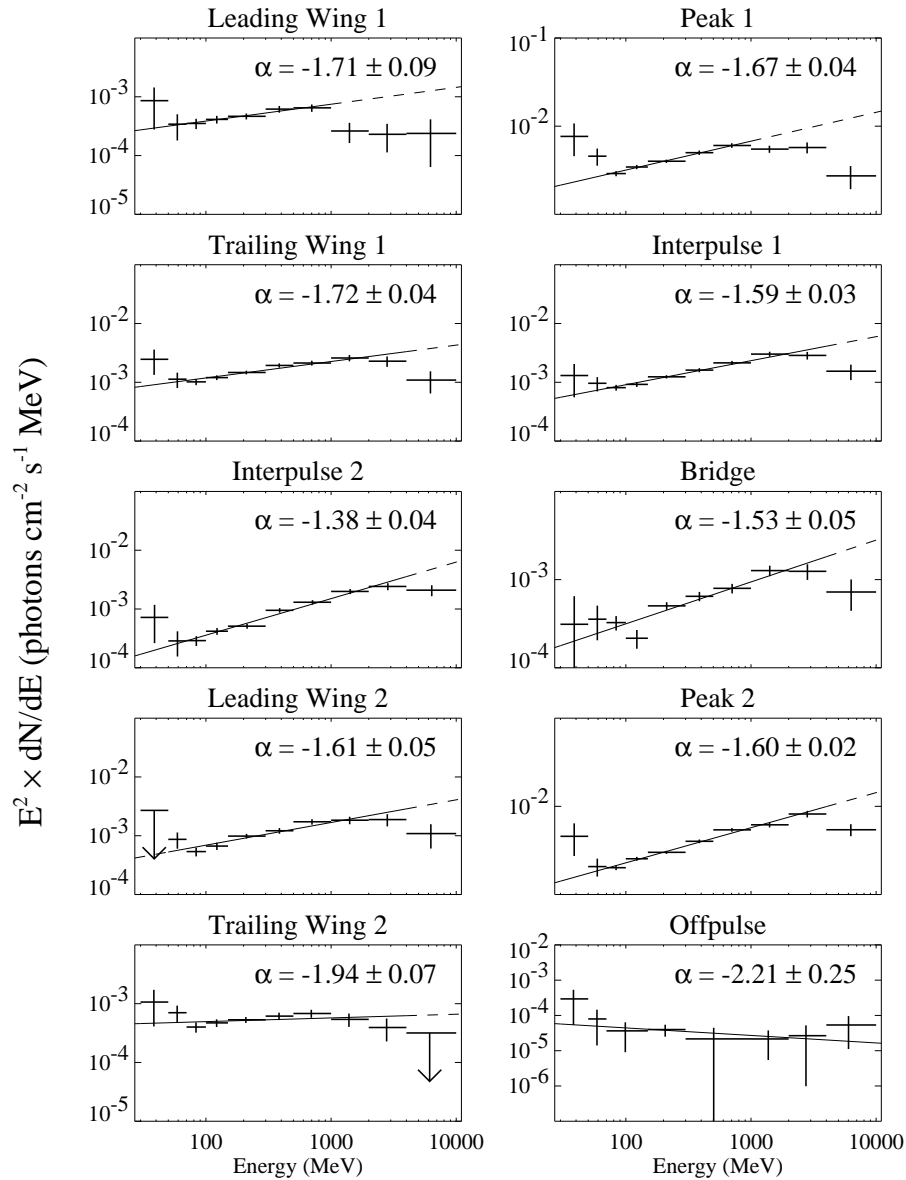


FIG. 11.—Instantaneous photon spectra derived from likelihood spatial analysis of the Vela pulse profile components defined in Table 6

Kanbach et al. (1994) exactly, the similarities of the two sets of phase-resolved spectra are evident.

## 5. DISCUSSION

### 5.1. Observational Results

A systematic, phase-resolved analysis of the total photon flux above 100 MeV reveals that the Crab, Geminga, and Vela pulsars all have significant emission in large portions of the off-pulse phase intervals. As opposed to studies of the Crab region, multiwavelength observations of Geminga and Vela give us no reason to believe that their off-pulse  $\gamma$ -ray emission might be due to nebular emission. If the Geminga and Vela pulsars are producing high-energy  $\gamma$ -ray emission throughout much of the rotation phase, then it is reasonable to assume that at least some of the emission in the Crab off-pulse region is also generated by the pulsar itself. It is worth noting that for all three pulse profiles, the lowest level of emission occurs just before the first  $\gamma$ -ray peak. While this

result is not statistically significant, it may be an early indication that the off-pulse emission is really composed of the extended tail(s) of the major  $\gamma$ -ray peaks.

Although it is not apparent from the phase histograms shown in the top panels of Figures 1, 2, and 3, phase-resolved analysis shows that the bridge emission is different for each of the three bright pulsars. Midway between its two peaks, the Crab bridge emission drops to an intensity level that is consistent with the weak emission in the off-pulse region. The Vela bridge emission also varies substantially but remains at a consistently high flux level and has a minimum very near the second peak. The emission from Geminga is both strong and relatively steady throughout the bridge region.

Despite the reduced photon statistics incurred by phase-resolved analysis, it is possible to acquire spectral information in most of the 20 phase bins by employing a hardness ratio such as that defined in equation (2). The Crab and Vela pulsar spectral variations are qualitatively similar in

that the hardness ratios increase smoothly through the first peak, have maximum values near the bridge region, and drop off after the second pulse. The Vela hardness ratios are typically greater than those of the Crab pulsar. Also, Vela becomes dramatically harder after the first pulse, an effect not seen in the Crab hardness ratios. In contrast to Crab and Vela, the hardness ratio for Geminga is strongly correlated with the features in its pulse profile. There are two broad plateaus corresponding to the first peak and bridge region, with an even larger hardness ratio at the location of the second peak. For all three pulsars, the softest ratios are in the off-pulse region.

Spectra derived from likelihood analysis of the individual pulse profile components confirm the behavior suggested by the distribution of hardness ratios. Of the three bright  $\gamma$ -ray pulsars, the softest emission occurs in the leading wing of the first Crab pulse, which has a measured spectral index of  $-2.65 \pm 0.15$ , with an almost identical spectral index measured for the trailing wing of the second pulse. The hardest pulsar component is the second peak from Geminga, which has a measured spectral index of  $-1.27 \pm 0.03$ . The latter part of the Vela interpulse component is almost as hard, with a measured spectral index of  $-1.38 \pm 0.04$ .

For all three pulsars, the component spectra share the same basic features as the total spectra. That is to say, the high-energy spectral turnovers that are apparent in the Vela and Geminga total spectra are also evident in the various component spectra. Likewise, the Crab profile components show the same soft emission at low energies that is apparent in the total Crab spectra, and only the leading peak shows some evidence of a high-energy turnover in its photon spectrum. Interestingly, for both the Vela and Geminga pulsars, the leading peak spectrum similarly turns over at a lower energy than the other pulsar components.

The four weakest Crab pulsar components are dominated by ultrasoft emission at energies below  $\sim 100$  MeV. Double power-law fits to the photon spectra from these four components show that the soft emission appears at roughly the same level in each component, with an average spectral index of  $-4.3 \pm 0.3$  and a flux of  $(1.1 \pm 0.1) \times 10^{-8}$  photons  $\text{cm}^{-2} \text{s}^{-1} \text{MeV}^{-1}$  at 100 MeV. This ultrasoft emission is also apparent in a double power-law fit to the total Crab emission, clearly indicating that it is an unpulsed component to the Crab  $\gamma$ -ray emission. It is not unreasonable to expect ultrasoft nebular emission out to energies on the order of  $\sim 100$  MeV. The emission at X-ray and soft  $\gamma$ -ray energies is consistent with synchrotron radiation produced by relativistic electrons streaming from the pulsar (Kennel & Coroniti 1984). Since the Crab pulsar is unlikely to produce electrons with energies greater than  $\sim 10^{15}$ – $10^{16}$  eV, the synchrotron spectrum will begin to roll over at energies above a few mega-electron volts. The soft emission observed from 30–100 MeV is then seen as the tail end of the synchrotron emission from the nebula. Detailed modeling of the Crab emission by de Jager et al. (1996) confirms this qualitative picture.

The detection of unpulsed emission from the Crab complex at teravolt energies (Weekes et al. 1989) implies that there is emission from the Crab Nebula beyond the synchrotron radiation. The teravolt emission is explainable in terms of inverse Compton scattering (de Jager et al. 1996), which has also been proposed as a possible explanation of the harder spectrum off-pulse emission above 1 GeV. However, based on the level of the teravolt emission, the

expected inverse Compton contribution at energies on the order of  $\sim 1$  GeV is below the EGRET flux measurements (Aharonian & Atoyan 1995). Considering the nonzero off-pulse emission seen from the Geminga and Vela pulsars, it is very likely that the bulk of the hard power-law component of the Crab off-pulse emission is generated by the pulsar itself.

## 5.2. Theoretical Implications

Original polar cap models of pulsar  $\gamma$ -ray emission (see, e.g., Harding 1981) suggested that double-peaked pulse profiles were produced by pulsars whose rotation axis was nearly orthogonal to its dipole axis. However, this could not explain peak separations much different than 0.5 in rotation phase or strong bridge emission between peaks. Since at least five of the six high-energy  $\gamma$ -ray pulsars have more than one peak (Ramanamurthy et al. 1995a; Fierro 1995; Thompson et al. 1996), it is unlikely that these are all orthogonal rotators whose beams cross the line of sight to the Earth. More recent incarnations of the polar cap models (see, e.g., Dermer & Sturmer 1994; Sturmer & Dermer 1994; Daugherty & Harding 1994) have made use of the fact that a pulsar with closely aligned rotation and magnetic axes pointed in the direction of the Earth will produce a hollow cone of emission from a single polar cap and result in two observed peaks, which correspond to when the line of sight from the Earth enters and exits the hollow cone. Yet phase-resolved analysis shows that all three bright  $\gamma$ -ray pulsars have emission across much of the rotation phase, which for the single pole outer gap model demands that the rotation and dipole axes have an aspect angle no greater than the radius of the polar cap cone of emission. For the narrow beaming angles associated with the standard polar cap model (see, e.g., Sturrock 1971), this suggests that there is a very large population of young, nearby neutron stars with closely aligned rotation and dipole axes.

Daugherty & Harding (1996) refined the single polar cap model by allowing the accelerating regions above the polar caps to extend out to heights on the order of a neutron star radius, significantly increasing the solid angle into which the cone of  $\gamma$ -ray emission is beamed. Not only does this make it more likely that a pulsar beam will cross the line of sight from the Earth, but it relaxes the requirement that the pulsar rotation and dipole axes be nearly aligned. Under these assumptions, Daugherty & Harding (1996) are able to closely reproduce the Vela pulse profile observed by EGRET, matching the narrow peak duty cycles, observed peak separation, and enhanced bridge emission. They also predict that there will be a finite level of emission outside of the two peaks due to residual high-altitude cascades. A natural consequence of this scenario is that the bridge emission will be harder than the peak emission because it comes from the interior of the polar cap, where the curvature radiation is less likely to cross magnetic field lines and be reprocessed into softer cascade photons. The emission outside of the peaks is due to high-altitude curvature radiation from electrons that have lost much of their peak energy, so this emission is expected to be the softest. It is also expected that the photon spectra from the peaks will turn over at lower energies than the spectra from the bridge regions because the peak emission will be more heavily attenuated by the magnetic field. It has already been noted that the leading peaks of the Crab, Vela, and Geminga pulsars have spectra that appear to turn over at lower energies than the other

pulsar components. While the measured hardness ratio distributions of the Crab and Vela pulsars qualitatively agree with the behavior expected for this polar cap scenario, the phase-resolved spectral behavior of the Geminga pulsar presents some problems. By far the hardest emission from Geminga comes from the second peak. Moreover, the emission between the peaks shows a sharper high-energy spectral turnover than the second peak. Both of these conditions indicate that the emission producing the second Geminga peak is not being significantly reprocessed to softer photons by the magnetic field.

The emission pattern of the magnetic Compton-induced pair cascade model (Dermer & Sturner 1994; Sturner & Dermer 1994) is similar to that of the curvature radiation-induced pair cascade model of Daugherty & Harding (1996), except that the high-energy  $\gamma$ -ray emission is produced close to the surface of the star, resulting in a much narrower  $\gamma$ -ray beam. In calculating the  $\gamma$ -ray spectral index as a function of pulsar phase, Sturner, Dermer, & Michel (1995) find that the hardest emission should come from the bridge region and the softest emission from the two peaks. This agrees somewhat with the observational results for the Crab and Vela pulsars—although the observed hardness ratios are not directly correlated with the peaks as suggested by Sturner et al. (1995)—but is in conflict with the extremely hard photon spectrum measured for the second  $\gamma$ -ray peak of Geminga. Moreover, the pulse profiles modeled by Sturner et al. (1995) do not reflect the narrow duty cycles of the peaks, strong bridge emission, or the significant off-pulse emission observed from the three brightest  $\gamma$ -ray pulsars.

Chiang & Romani (1992) found that outer gap emission from a single pole produces a broad, irregularly shaped beam of emission that is particularly dense near the edges, so that two  $\gamma$ -ray peaks are observed when the line of sight from the Earth crosses these enhanced regions of the  $\gamma$ -ray beam, while the inner region of the beam provides a significant amount of emission between the peaks. A wide range of peak phase separations can be accommodated with a proper choice of the observer colatitude. Double-peaked pulse profiles of varying phase separation and strong bridge emission occur naturally in this model. The nonzero off-pulse emission can be seen as resulting from residual pair cascades high in the outer magnetosphere. Because of the complex geometry and interaction of emission processes in the outer magnetosphere, no detailed spectra or luminosities have been modeled for the single pole outer gap model.

A clue to the nature of pulsar  $\gamma$ -ray emission may come from the fact that for each of the three bright  $\gamma$ -ray pulsars, the individual component spectra have similar high-energy turnovers, when the turnovers are detectable. Magnetic field attenuation would be a likely cause of the spectral turnovers if the various pulsar components are being generated close to the surface of the neutron star, where the local magnetic field is strong. However, if the turnovers are due to attenuation by the magnetic field, the Crab pulsar, with an inferred surface magnetic field of  $3.7 \times 10^{12}$  G, should show a sharper spectral break than a weaker field pulsar like Geminga, which has an inferred surface magnetic field of  $1.6 \times 10^{12}$  G. It is also possible that the spectral turnovers are the result of a cutoff in the source distribution of

charged particles at high energies. Assuming that the maximum energy attainable by a charged particle is directly related to the maximum potential drop of the pulsar, which goes as  $\Delta\Phi \propto BP^{-2}$ , where  $B$  is the surface magnetic field and  $P$  is the rotation period of the pulsar, one would expect the Crab pulsar to have the highest charged particle distribution turnover energy among the three bright  $\gamma$ -ray pulsars, while Geminga should have the lowest. This could be why the Crab photon spectrum shows no strong spectral turnover below 10 GeV, while Geminga has a sharp turnover. On the other hand, PSR B1951+32, with a  $\Delta\Phi$  lower than that of the Vela pulsar, shows no high-energy cutoff (Ramanamurthy et al. 1995a).

A spectral turnover caused by a dropoff in the distribution of primary charged particles at high energies will be reflected in both the total emission photon spectrum and the individual component spectra. However, it is not clear why the first peak of the  $\gamma$ -ray pulsars seems to have a slightly stronger cutoff than do the other pulsar components. Perhaps the first peak originates closer to the surface of the pulsar where the local magnetic field is stronger and there is a higher degree of magnetic field attenuation, but then it might be expected that the first peak should be softer than the other components due to the significant reprocessing of high-energy photons to lower energies. While Vela and Geminga have somewhat softer leading peaks, the Crab pulsar does not.

Even though there is some question as to the exact location in the magnetosphere where each pulse profile component is generated, the significant variation in hardness ratio as a function of rotation phase indicates that the line of sight to the pulsar is sweeping across field lines with a broad range in curvature radii. Most likely, the softest components come from the regions with the most curved field lines. The two peaks of the Crab and Vela pulsars are softer than the bridge regions, which suggests that the peaks might be at least partially caused by the increase in curvature radiation one would expect along the most curved field lines. Yet the second peak of Geminga, which is actually the stronger peak, has the hardest measured spectral index of any object or pulsar component observed by EGRET. Either the primary charged particle distribution responsible for this peak has a very enhanced, flat number spectrum, or, more plausibly, the second Geminga peak results from inverse Compton scattering, which can reasonably produce an intense, hard photon spectrum. The second peak of Geminga appears to be direct evidence that processes besides curvature radiation and synchrotron radiation are playing an important role in the pulsar magnetosphere.

The authors would like to thank R. Romani for his helpful discussions regarding the soft emission in the Crab total spectrum. We thank the referee, H. Mayer-Hasselwander, for his helpful comments.

The EGRET team gratefully acknowledges support from the following: NASA grant NAG5-1605 (S. U.), NASA Cooperative Agreement NCC 5-95 (H. S. C.), NASA contract NAS5-96051 (N. G. C.), Bundesministerium für Bildung, Wissenschaft, Forschung und Technologie grant 50 QV 9095 (M. P. E.), and Deutsche Forschungsgemeinschaft (Sonderforschungsbereich 328).

## REFERENCES

- Aharonian, F. A., & Atoyan, A. M. 1995, *Astropart. Phys.*, 3, N3
- Arzoumanian, Z., Nice, D., & Taylor, J. H. 1992, *GRO/Radio Timing Database*, Princeton University
- Bertsch, D. L., et al. 1989, in *Proc. of the Gamma-Ray Observatory Science Workshop*, ed. W. N. Johnson (Greenbelt, MD: Goddard Space Flight Center), 2-52
- Bertsch, D. L., Dame, T. M., Fichtel, C. E., Hunter, S. D., Sreekumar, P., Stacy, J. G., & Thaddeus, P. 1993, *ApJ*, 416, 587
- Cheng, K. S., Ho, C., & Ruderman, M. 1986a, *ApJ*, 300, 500
- . 1986b, *ApJ*, 300, 522
- Chiang, J., & Romani, R. W. 1992, *ApJ*, 400, 629
- Clear, J., Bennett, K., Buccheri, R., Grenier, I. A., Hermesen, W., Mayer-Hasselwander, H. A., & Sacco, B. 1987, *A&A*, 174, 85
- Daugherty, J. K., & Harding, A. K. 1994, *ApJ*, 429, 325
- . 1996, *ApJ*, 458, 278
- de Jager, O. C., Harding, A. K., Michelson, P. F., Nel, H. I., Nolan, P. L., Sreekumar, P., & Thompson, D. J. 1996, *ApJ*, 457, 253
- de Jager, O. C., Harding, A. K., & Strickman, M. S. 1996, *ApJ*, 460, 729
- Dermer, C. D., & Sturmer, S. J. 1994, *ApJ*, 420, L75
- Esposito, J. A., et al. 1998, in preparation
- Fierro, J. M. 1995, Ph.D. thesis, Stanford University
- Grenier, I. A., Hermesen, W., & Clear, J. 1988, *A&A*, 204, 117
- Harding, A. K. 1981, *ApJ*, 245, 267
- Hughes, E. B., et al. 1980, *IEEE Trans. Nucl. Sci.*, NS-27, 364
- Hunter, S. D., et al. 1997, *ApJ*, 481, 205
- Kanbach, G., et al. 1988, *Space Sci. Rev.*, 49, 69
- Kanbach, G., et al. 1989, in *Proc. of the Gamma-Ray Observatory Science Workshop*, ed. W. N. Johnson (Greenbelt, MD: Goddard Space Flight Center), 2-1
- Kanbach, G., et al. 1993, *A&AS*, 97, 349
- . 1994, *A&A*, 289, 855
- Kennel, C. F., & Coroniti, F. V. 1984, *ApJ*, 283, 694
- Mattox, J. R. 1994, in *AIP Conf. Proc. 304, The Second Compton Symposium*, ed. C. E. Fichtel et al. (New York: AIP), 77
- Mattox, J. R., et al. 1996, *ApJ*, 461, 396
- McLaughlin, M. A., Mattox, J. R., Cordes, J. M., & Thompson, D. J. 1996, *ApJ*, 473, 763
- Mayer-Hasselwander, H. A., et al. 1994, *ApJ*, 421, 276
- Nolan, P. L., et al. 1992, *IEEE Trans. Nucl. Sci.*, 39, 993
- . 1993, *ApJ*, 409, 697
- Ramanamurthy, P. V., et al. 1995a, *ApJ*, 447, L109
- . 1995b, *ApJ*, 450, 791
- Romani, R. W., & Yadigaroglu, I.-A. 1995, *ApJ*, 438, 314
- Sturmer, S. J. 1995, *ApJ*, 446, 292
- Sturmer, S. J., & Dermer, C. D. 1994a, *ApJ*, 420, L79
- Sturmer, S. J., Dermer, C. D., & Michel, F. C. 1995, *ApJ*, 445, 736
- Sturrock, P. A. 1971, *ApJ*, 164, 529
- Thompson, D. J., et al. 1993, *ApJS*, 86, 629
- Thompson, D. J., et al. 1995, *ApJS*, 101, 259
- . 1996, *ApJ*, 465, 385
- Vacanti, G., et al. 1991, *ApJ*, 377, 467
- Weekes, T. C., et al. 1989, *ApJ*, 342, 379
- Yadigaroglu, I.-A., & Romani, R. W. 1995, *ApJ*, 449, 211